Incompletely Decomposed In$_4$SnSe$_4$ Leads to High-Ranged Thermoelectric Performance in n-Type PbTe

Haonan Shi, Yongxin Qin, Bingchao Qin, Lizhong Su, Yuping Wang, Yongjin Chen, Xiang Gao, Hao Liang, Zhen-Hua Ge, Tao Hong,* and Li-Dong Zhao*

Additives in thermoelectric materials are conventionally considered as either extrinsic defects or second phases regardless of their dynamic processes. Herein, In$_4$SnSe$_4$, with inherent low thermal conductivity, is introduced into n-type PbTe. It is revealed that In$_4$SnSe$_4$ decomposes incompletely at high temperatures, in which around 80% of In$_4$SnSe$_4$ dissolves into InSe and Sn, while 20% forms as nano-precipitates. Benefiting from the incomplete decomposition, PbTe-0.1%In$_4$SnSe$_4$ presents superior thermoelectric performance compared to the stepwise and compositionally identical PbTe-0.4%InSe-0.1%Sn. The residual In$_4$SnSe$_4$ along with Sn and InSe jointly contribute to the synergetic optimization of carrier mobility and lattice thermal conductivity in PbTe-0.1%In$_4$SnSe$_4$. As a result, the room-temperature dimensionless figure of merit (ZT) of ≈0.4 and the ZT$_{ave}$ of ≈0.83 at 300–573 K are obtained, and an experimental maximum thermoelectric conversion efficiency (η) of ≈2.5% (ΔT ≈ 400 K) is obtained, demonstrating significant research progress in n-type PbTe. This work indicates that the In$_4$SnSe$_4$ incomplete decomposition effectively decouples the electron and phonon transports in n-type PbTe and the strategy of utilizing the unstable additives is proven feasible. Additionally, more dynamic behaviors of additives are worth expecting and may promote more achievements for other thermoelectric systems.

H. Shi, Y. Qin, B. Qin, L. Su, Y. Wang, T. Hong, L.-D. Zhao
School of Materials Science and Engineering
Beihang University
Beijing 100191, China
E-mail: hongtao77@buaa.edu.cn; zhaolidong@buaa.edu.cn
Y. Chen, X. Gao
Center for High Pressure Science and Technology
Advanced Research (HPSTAR)
Beijing 100094, China
H. Liang, Z.-H. Ge
Faculty of Materials Science and Engineering
Kunming University of Science and Technology
Kunming 650093, China
L.-D. Zhao
Key Laboratory of Intelligent Sensing Materials and Chip Integration
Technology of Zhejiang Province (2021E10022)
Hangzhou Innovation Institute of Beihang University
Hangzhou 310051, China

1. Introduction

Thermoelectric materials and their technologies, as emerging green energy technologies in recent years, have been regarded as the key means to solving the global energy crisis. Thermoelectric materials can realize the energy conversion between electricity and heat, which are expected to be utilized for waste heat harvesting and solid-state cooling.[1] The conversion efficiency of thermoelectric materials is determined by the dimensionless figure of merit (ZT), namely $ZT = S^2\sigma T/\kappa_{tot}$, where S, σ, T and κ_{tot} are Seebeck coefficient, electrical conductivity, absolute temperature, and total thermal conductivity, respectively.[2] Therefore, excellent thermoelectric performance requires a large Seebeck coefficient, high electrical conductivity, and low thermal conductivity. However, the interdependence of thermoelectric parameters limits the enhancement of the ZT value. To obtain high performance, it is the priority to balance the strongly coupled parameters by decoupling the electron and phonon transports.[3]

Researchers have proposed many effective strategies such as band convergence,[4] resonant levels,[5] and symmetry manipulation[6] for the improvement of electrical transport, and all-scale hierarchical architectures[7] and the search for materials with intrinsically low thermal conductivity[8] for the suppression of thermal transport. From the perspective of the compositions and microstructures of samples, the above strategies can be implemented mainly in two ways. One is alloying or doping impurity elements, like Pb-alloyed SnSe,[3a,9] Se-alloyed PbTe,[10] and Cd-doped AgSbTe$_2$.[11] The other is introducing second phases, like MnTe-Sb$_2$Te$_3$,[12] CuGaTe$_2$-Ag$_2$Te,[13] and PbSe-SiO$_2$.[14] Generally, the elemental doping and alloying mainly optimize the electrical transport by tuning the carrier density and mobility or modifying the electronic band structure, while the induced second phases contribute to suppressing the thermal transport by strengthening the defects-phonon scattering.

Considering the synthesis process of samples, the additives are introduced into the matrix by simply using either pure elements for doping and alloying or target compounds for the second phases, while both kinds of additives are considered to

be in steady states. For example, in SnSe–AgSb(Se/Te)$_2$ system, the elementary substances of all required elements are mixed together when sample synthesizing, instead of mixing compounds SnSe and AgSb(Se/Te)$_2$,[15] while taking PbS–Cu$_2$S,[16] and PbSe–CdTe[17] systems as examples, the binary compounds as second phases were directly added to the matrix materials. However, not all compounds keep chemically stable in the matrix and some potentially dynamic behaviors such as intrinsic decomposition and reaction with the matrix of multielement additives can generate significant impacts on thermoelectric performance. Especially, the compounds with intrinsically low thermal conductivity are rather crucial as second phases to depress the thermal transport of the matrix, while they are also mostly possessing complex and unstable structures and phases.[1b]

PbTe, as a typical mid-temperature thermoelectric material, has been continuously studied over a semicentury.[16,18] However, the high thermal conductivity is an important factor limiting its thermoelectric conversion efficiency. In this work, the additive compound In$_4$SnSe$_4$, which has been proven to possess intrinsically low thermal conductivity in our previous work,[19] was selected as the second phase in n-type PbTe. To note, all samples in this work were doped with 0.4% iodine to realize the n-type transport in PbTe. Resultantly, the thermal conductivity was largely reduced by introducing In$_4$SnSe$_4$ as expected. However, the anomalous trend of electrical conductivity indicated that In$_4$SnSe$_4$ did not only act as a second phase. By structural and phase analysis, we discovered that an incomplete decomposition of In$_4$SnSe$_4$ happened at ≈1163 K, which is lower than the melting temperature of PbTe during synthesis (≈1300 K). Quantitative analysis from the X-ray diffraction (XRD) refinement showed that around 80% of In$_4$SnSe$_4$ decomposed into InSe and Sn, while the other 20% remained as In$_4$SnSe$_4$ second phases in the PbTe matrix. The obvious coexistence of In$_4$SnSe$_4$, InSe, and Sn in the PbTe-0.1% In$_4$SnSe$_4$ sample directly observed by Cs-corrected STEM characterizations proved the incomplete decomposition of In$_4$SnSe$_4$ in PbTe. To further investigate the effect of the decomposition process of In$_4$SnSe$_4$ on the thermoelectric performance of PbTe, we compared the properties of PbTe-0.1%In$_4$SnSe$_4$ and PbTe-0.4%InSe-0.1%Sn with the identical nominal composition. Surprisingly, PbTe-0.1%In$_4$SnSe$_4$ presented higher carrier mobility of ≈1209 cm^2 V^{-1} s^{-1} and lower lattice thermal conductivity of ≈1.5 W m^{-1} K^{-1} at 300 K, which were more excellent than those of PbTe-0.4%InSe-0.1%Sn (≈674 cm^2 V^{-1} s^{-1} and ≈2.1 W m^{-1} K^{-1}). The semi-coherent interfaces formed between undecomposed In$_4$SnSe$_4$ nano-precipitates and PbTe matrix reduced the carrier scattering and distorted the crystal lattice in PbTe-0.1%In$_4$SnSe$_4$, synergistically optimizing the electron and phonon transports. As a result, a high ZT value of ≈0.4 at 300 K with an average ZT (ZT_{ave}) ≈0.83 at 300–573 K in PbTe-0.1%In$_4$SnSe$_4$ were obtained, demonstrating significant advantages over the reported n-type PbTe thermoelectrics.

2. Results and Discussion

2.1. In$_4$SnSe$_4$ Introduced into n-Type PbTe

In$_4$SnSe$_4$ is an intrinsic low thermal conductivity material with a cubic structure, which has been reported in our previous work.[19]

Figure S14, Supporting Information, shows the comparison of the thermal conductivities between In$_4$SnSe$_4$ and n-type PbTe. It can be seen that In$_4$SnSe$_4$ may be a suitable second phase for PbTe because of the similar cubic structure and lower thermal conductivity. Therefore, to suppress the heat transport in n-type PbTe, In$_4$SnSe$_4$ is introduced into 0.4% I-doped PbTe (abbreviated as PbTe in the following discussion) as a second phase. The XRD patterns and lattice parameters are shown in Figure S2a,b, Supporting Information. All samples are indexed into a single *P1* phase and no obvious changes are observed in lattice parameters due to the low addition of In$_4$SnSe$_4$. **Figure 1** shows the electrical transport properties of PbTe-x%In$_4$SnSe$_4$ (x = 0, 0.04, 0.06, 0.08, 0.10, 0.12, 0.14) samples. The electrical conductivity (σ) presents a downward trend when $x \geq 0.10$ in Figure 1a and the absolute value of Seebeck coefficient (S) is enhanced with the increasing In$_4$SnSe$_4$ content in Figure 1b. The carrier concentration (n) decreases from 2.85×10^{19} ($x = 0$) to 7.29×10^{18} cm^{-3} ($x = 0.14$) as shown in Figure 1c. Accordingly, the carrier mobility boosts obviously and exceeds ≈1000 cm^2 V^{-1} s^{-1} when $x \geq 0.10$. As a result, the power factor (PF) shown in Figure 1d is enhanced in the entire temperature range especially at room temperature, which is increased from ≈10 ($x = 0$) to 33 μW cm^{-1} K^{-2} ($x = 0.10$) at 300 K.

The thermal transport properties of PbTe-x%In$_4$SnSe$_4$ samples are illustrated in **Figure 2**a,b and Figure S3, Supporting Information. The densities of PbTe-x%In$_4$SnSe$_4$ samples are listed in Table S1, Supporting Information. As shown in Figure 2b, the In$_4$SnSe$_4$-added samples present a declining lattice thermal conductivity (κ_{lat}) as expected. The κ_{lat} reaches ≈1.5 W m^{-1} K^{-1} after the addition of In$_4$SnSe$_4$, which is ≈45% lower than the In$_4$SnSe$_4$-free sample. Combining with the decreased electronic thermal conductivity (κ_{ele}), the total thermal conductivity (κ_{tot}) falls prominently from ≈4.2 ($x = 0$) to 2.5 W m^{-1} K^{-1} ($x = 0.10$) in Figure 2a. Figure 2c shows the μ/κ_{lat} at 300 K of PbTe-x%In$_4$SnSe$_4$ samples. The boosted value of μ/κ_{lat} indicates that electron and phonon transports are well decoupled in n-type PbTe after In$_4$SnSe$_4$ adding[20] and the ZT value is promoted to ≈0.4 at 300 K in PbTe-0.1%In$_4$SnSe$_4$, as shown in Figure 2d.

The enhanced thermoelectric properties motivate us to shed light on the optimization mechanism of In$_4$SnSe$_4$ in n-type PbTe. It is noteworthy that the electrical conductivity of PbTe-x%In$_4$SnSe$_4$ samples undergoes an extraordinary trend in Figure 1a, which increases obviously when $x < 0.10$. It has been confirmed that In$_4$SnSe$_4$, with a wide bandgap of ≈1.54 eV, is poor in electrical conduction.[19,21] That is, the nearly electrically insulated In$_4$SnSe$_4$ leads to an elevated electrical conductivity in n-type PbTe when $x < 0.10$, which is contrary to the conventional perception. Therefore, the role of In$_4$SnSe$_4$ in n-type PbTe needs to be further investigated, which is not simply as a precipitate phase.

2.2. Incomplete Decomposition of In$_4$SnSe$_4$

The decomposition behavior has been found in some multi-element compounds while heating, such as Cs$_4$Cu$_3$Bi$_9$S$_{17}$[22] and CdMBi$_4$Se$_8$ (M = Sn or Pb).[23] For In$_4$SnSe$_4$, it is possible that the decomposition also occurs and the decomposed products may lead to the extraordinary enhancement of electrical
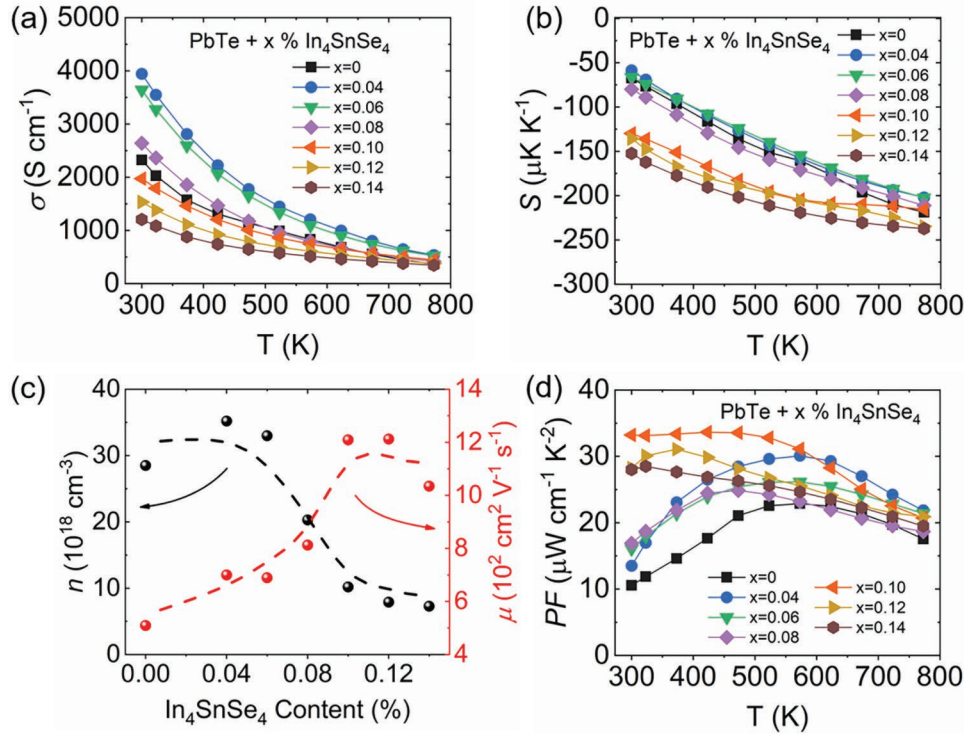
Figure 1. Electrical transport properties as a function of temperature in PbTe-x%In$_4$SnSe$_4$ (x = 0–0.14): a) electrical conductivity; b) Seebeck coefficient; c) carrier concentration and carrier mobility as a function of In$_4$SnSe$_4$ content; d) power factor.
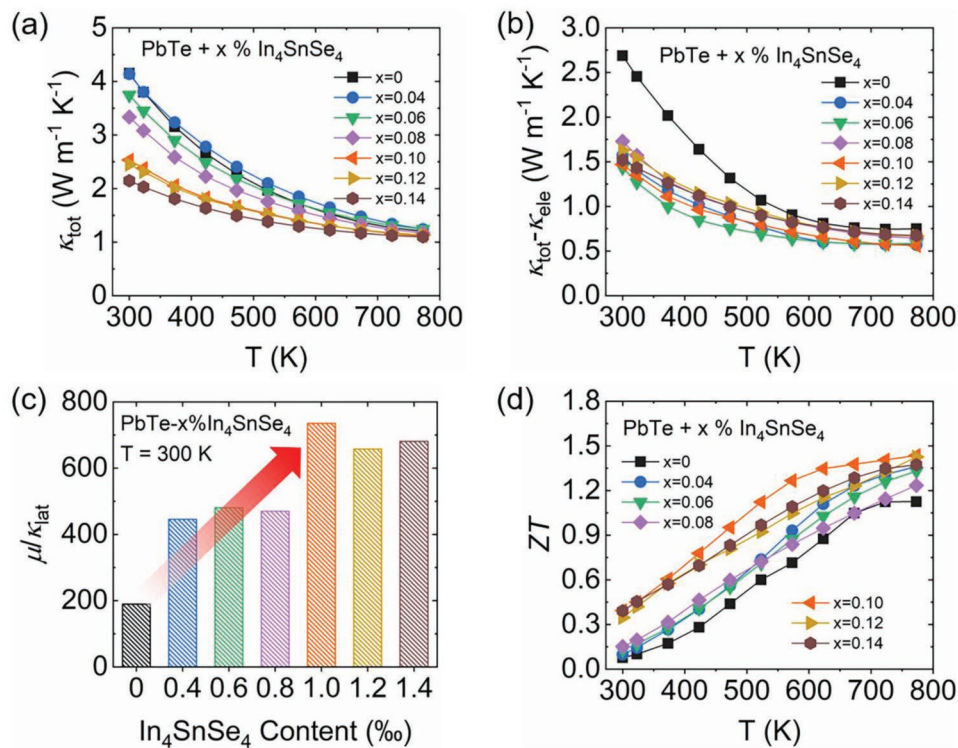
Figure 2. Thermal transport properties and ZT values as a function of temperature in PbTe-x%In$_4$SnSe$_4$ (x = 0–0.14): a) total thermal conductivity; b) lattice thermal conductivity; c) the ratio of carrier mobility to lattice thermal conductivity as a function of In$_4$SnSe$_4$ content at 300 K; d) ZT values.
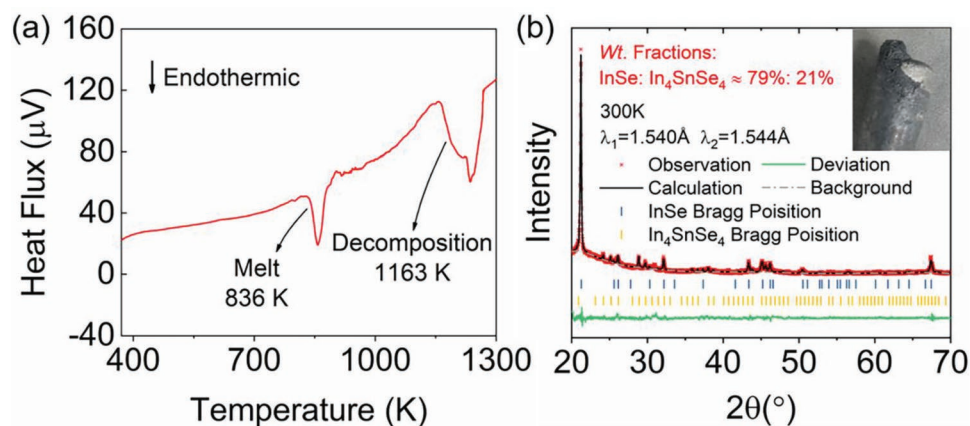
Figure 3. The research of the decomposition process in In_4SnSe_4: a) the differential scanning calorimetry (DSC) curve of In_4SnSe_4 from 400 to 1300 K; b) the refined XRD pattern of after-heated In_4SnSe_4, the inset is the photo of the In_4SnSe_4 which has been heated to 1300 K and cooled.

conductivity in PbTe as mentioned above. To reveal the thermal behavior of In_4SnSe_4, differential scanning calorimetry (DSC) is carried out as shown in **Figure 3**a. In order to be consistent with the synthesis temperature of the PbTe-x%In_4SnSe_4 samples (1300 K, see Figure S1, Supporting Information), the temperature range of the DSC measurement is set to 400–1300 K. The result shows that In_4SnSe_4 undergoes two endothermic processes during the measurement. The first peak at ≈836 K is attributed to the melting of In_4SnSe_4,[19,24] while the second peak at ≈1163 K indicates another unknown endothermic process, which may correspond to the decomposition of In_4SnSe_4.

To clarify the origin of the endothermic peak at ≈1163 K, the powder X-ray diffraction (PXRD) of the after-heated In_4SnSe_4 is carried out (see Section 1.2, Supporting Information). The photo of after-heated In_4SnSe_4 is exhibited in the inset of Figure 3b and a suspected tin precipitate is found on the top of the ingot due to its white color and excellent softness. The result of PXRD and the Rietveld refinements in Figure 3b suggests that InSe and In_4SnSe_4 coexist in the after-heated ingot, whose weighted fractions are 79% and 21%, respectively. It strongly indicates that the endothermic peak at ≈1163 K can be ascribed to the incomplete decomposition of In_4SnSe_4 ($In_4SnSe_4 \rightarrow 4InSe + Sn$). Moreover, the previous work also suggested that In_4SnSe_4 is mostly inclined to break down into InSe and Sn based on the calculation of decomposition energy.[21b] As a result, it can be confirmed that the endothermic peak at ≈1163 K in the DSC measurement is caused by the decomposition of In_4SnSe_4. And this process is not complete, whose decomposition ratio is ≈81.3% calculated by the weighted fractions and molar ratio.

To assess the role of In_4SnSe_4 in n-type PbTe, microstructure characterizations are carried out. Figure S4, Supporting Information, shows the scanning electron microscope (SEM) images of the PbTe-0.1%In_4SnSe_4 sample and no second phases on the micrometer scale are observed, which is consistent with the result of XRD.[25] Therefore, to further reveal the present state of the In_4SnSe_4 in the PbTe matrix, we conduct a scanning transmission electron microscopy (STEM) study with a Cs-corrected TEM. **Figure 4**a shows the microscopic morphological phases of the PbTe-0.1%In_4SnSe_4 sample, and Figure 4b demonstrates the presence of a large number of nano-precipitates in it. Figure 4c shows the elemental analysis of the

corresponding energy dispersive spectroscopy (EDS) mapping images of Figure 4b, which display the enrichments of In and Sn elements. However, the energy difference between Sn and In peaks is less than the energy resolution of the EDS mapping probe, since the characteristic peaks of $L\alpha_1$ and $L\alpha_2$ of In are at 3.286 and 3.487 keV, which are very close to the characteristic peak of Sn at 3.444 keV (see Table S4, Supporting Information). This is why the enrichments of Sn and In almost overlap with each other. To distinguish the characteristics of these nano-precipitates, a more detailed study and description are needed.

An annular dark-field STEM (ADF-STEM) image of a nano-precipitate in PbTe-0.1%In_4SnSe_4 is shown in Figure 4d. A laminar arrangement can be founded in it, which possesses a much lower crystallographic spacing. Figure 4e depicts a Fast Fourier Transform (FFT) image of Figure 4d, which clearly indicates the electron diffraction spots in the [100] axis of the PbTe matrix and some additional diffraction spots belonging to the nano-precipitate. The calculated crystal spacing of the nano-precipitate is ≈0.70 Å, which is consistent with that of InSe. Combined with the layered structure in Figure 4d, these extra spots are calibrated and judged as diffraction spots of InSe in the [100] direction.

Figure 4f shows the high-angle annular dark-field STEM (HAADF-STEM) image at the boundary between another nano-precipitate and the PbTe matrix in PbTe-0.1%In_4SnSe_4, and the region around the boundary is enlarged in Figure 4g. The inset in Figure 4g indicates the crystal structure of In_4SnSe_4 in the [111] axis, which agrees well with the experimental atomic arrangements at most sites but deviates to some extent at other sites due to the distortion. It can be seen in Figure 4f that the arrangement of the In_4SnSe_4 precipitates at the boundary is different from which inside because the PbTe matrix exerts high stress on the nano-precipitates and the arrangement of In_4SnSe_4 is distorted around the boundary. As a result, it can be proved that In_4SnSe_4 also exists in PbTe-0.1%In_4SnSe_4.

In order to further distinguish the different precipitates and remedy the insufficient energy resolution of the EDS mapping, we have performed an electron energy loss spectroscopy (EELS) analysis on a nano-precipitate at the edge, as shown in Figure 4h. It can be seen that the outer layer of the nano-precipitate has a clear laminar arrangement (marked by the
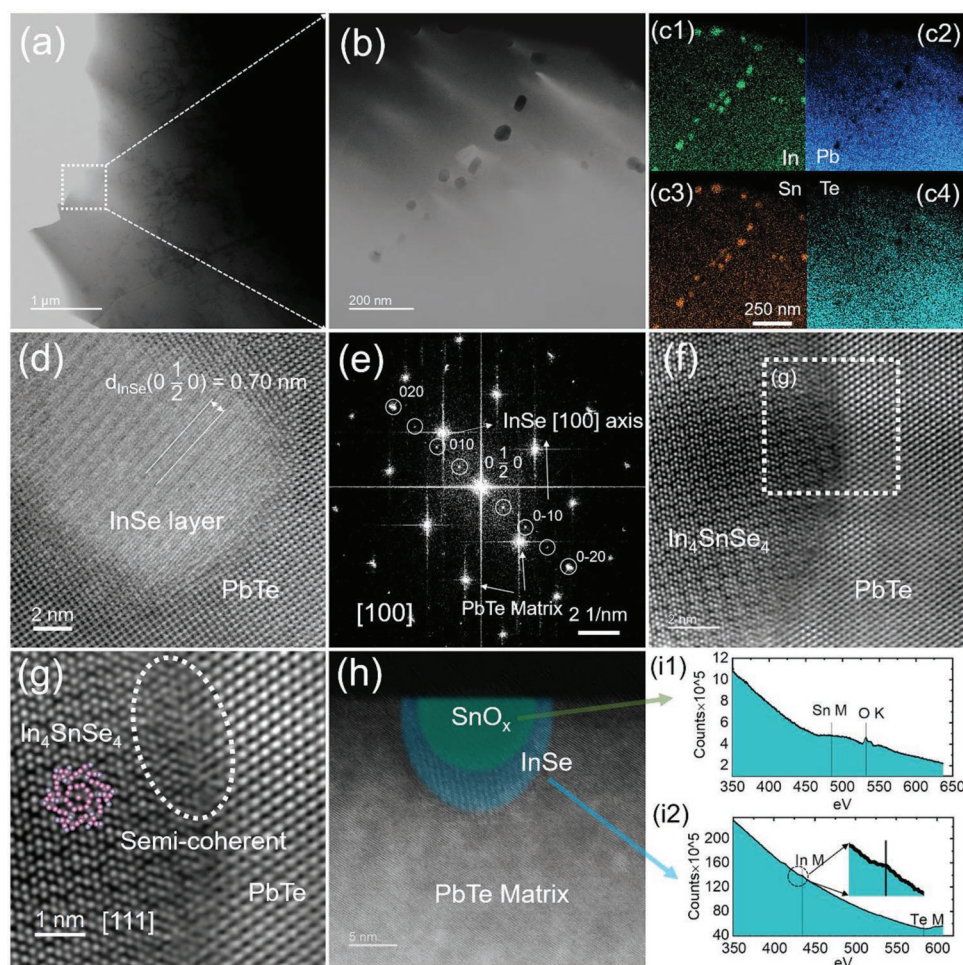
Figure 4. Microstructure observation in PbTe-0.1%In$_4$SnSe$_4$: a) low-magnification ADF-STEM image showing the morphology of the sample; b) middle-magnification ADF-STEM image showing the formation of considerable nanoprecipitates; c1–c4) the corresponding energy-dispersive X-ray spectroscopy (EDS) mappings of (b); d) ABF-STEM image showing the presence of a layered structure nanoprecipitate in the PbTe matrix; e) the Fast Fourier Transform (FFT) image shows the diffraction spots in the [100] direction of the PbTe matrix, but also the diffraction spots in the [100] axis of the layered InSe (marked by the white circles); f) atomic-scale HAADF-STEM image demonstrating a In$_4$SnSe$_4$ nanoprecipitate in the PbTe matrix; g) the enlarged image of (f) displaying the semi-coherent interface between the In$_4$SnSe$_4$ and the PbTe matrix, the inset is the In$_4$SnSe$_4$ crystal structure from [111] axis; h) ADF-STEM image illustrating the decomposition products Sn (oxidized to SnO$_x$ at the edge) and InSe of In$_4$SnSe$_4$; i1–i2) the electron energy loss spectra (EELS) separately collected from the region of (h), (i1) exhibits the distinct energy loss peaks for Sn M and O K, and (i2) exhibits energy loss peaks for In M.

blue area), while the inner green area does not possess such a laminar structure. The EELS spectra are shown in Figure 4i1,i2. The energy loss peaks of Sn M and O K are visible in Figure 4i1, since the decomposition product Sn around the edge is oxidized by the oxygen in the air. Figure 4i2 shows the EELS spectrum of the lamellar region in Figure 4h. There is a distinctive energy loss peak of In M (enlarged in the inset), which can be determined as InSe in combination with the previous results. This is also consistent with the results in Figure 4d,e. Thus, the region in Figure 4h shows the coexistence of InSe and Sn, which can be considered as direct evidence for the decomposition of In$_4$SnSe$_4$ in the PbTe matrix.

In summary, the results of thermal analysis, phase refinement, and microstructure observation collectively confirm that an incomplete decomposition of In$_4$SnSe$_4$ (In$_4$SnSe$_4 \rightarrow$ 4InSe + Sn) happens at high temperatures. This dynamic process can also

proceed in the PbTe matrix and the products (InSe, Sn, and residual In$_4$SnSe$_4$) all exist in PbTe-0.1% In$_4$SnSe$_4$.

2.3. The Comparison of PbTe-0.1%In$_4$SnSe$_4$ and PbTe-0.4%InSe-0.1%Sn

As discussed above, InSe and Sn are produced in PbTe after In$_4$SnSe$_4$ adding, and the undecomposed In$_4$SnSe$_4$ also remains in the matrix. To methodically clarify the complex mechanism generated by the In$_4$SnSe$_4$ additive, the decomposition products InSe and Sn are successively added to PbTe.

First, the PbTe-γ%InSe (γ = 0, 0.2, 0.3, 0.4, 0.5) samples are prepared and the XRD patterns are showed in Figure S2c,d, Supporting Information. The addition of InSe strongly scatters phonons and leads to a decreased κ_{lat}, from ≈2.7 W m^{-1} K^{-1} in

ADVANCED
SCIENCE NEWS
www.advancedsciencenews.com

ADVANCED
ENERGY
MATERIALS
www.advenergymat.de

InSe-free PbTe to ≈2.0 W m^{-1} K^{-1} in PbTe-0.4%InSe as shown in Figure S11e, Supporting Information. Meanwhile, as a poor conductor, InSe causes the reduction of electrical conductivity and the concomitantly increased Seebeck coefficient.[26] The carrier concentration is adjusted to a more appropriate value for n-type PbTe and the power factors of PbTe-γ%InSe are enhanced at room and middle temperature ranges. With the optimized carrier concentration and suppressed lattice thermal conductivity, the *ZT* values of InSe-added PbTe are obviously enhanced. The thermoelectric properties and densities of PbTe-γ%InSe samples are shown in Figures S10 and S11; and Table S2, Supporting Information.

Subsequently, another decomposition product Sn is added to PbTe-0.4%InSe. The XRD patterns of all PbTe-0.4%InSe-*z*%Sn (*z* = 0, 0.05, 0.1, 0.2, 0.3) samples show no abnormality in Figure S2e,f, Supporting Information. The Sn atoms enter the PbTe matrix and fill in the natural Pb vacancies, decreasing the concentration of holes.[27] Thus, the addition of Sn realizes an

n-type alloying, leading to the slightly increased carrier concentration in Figure S12c, Supporting Information. The occupied Pb vacancies attenuate the scattering of carriers (electrons), thereby boosting the carrier mobility. Meanwhile, the total thermal conductivities become higher due to the increased electronic thermal conductivities. Finally, the *ZT* value is further enhanced in PbTe-0.4%InSe-0.1%Sn. More details of PbTe-0.4%InSe-*z*%Sn samples are shown in Figures S12 and S13; and Table S3, Supporting Information.

To further comprehend the role of In$_4$SnSe$_4$ additive in n-type PbTe, the properties of three optimal samples, PbTe-0.4%InSe, PbTe-0.4%InSe-0.1%Sn, and PbTe-0.1%In$_4$SnSe$_4$ are exhibited in **Figure 5**, and the In$_4$SnSe$_4$-free PbTe is also shown as a comparison. As discussed above, InSe suppresses the heat transport and Sn accelerates the electron transport in n-type PbTe. However, it is counterintuitive that PbTe-0.1%In$_4$SnSe$_4$ and PbTe-0.4%InSe-0.1%Sn, which possess nominally the same composition, present a huge difference in both electrical and thermal
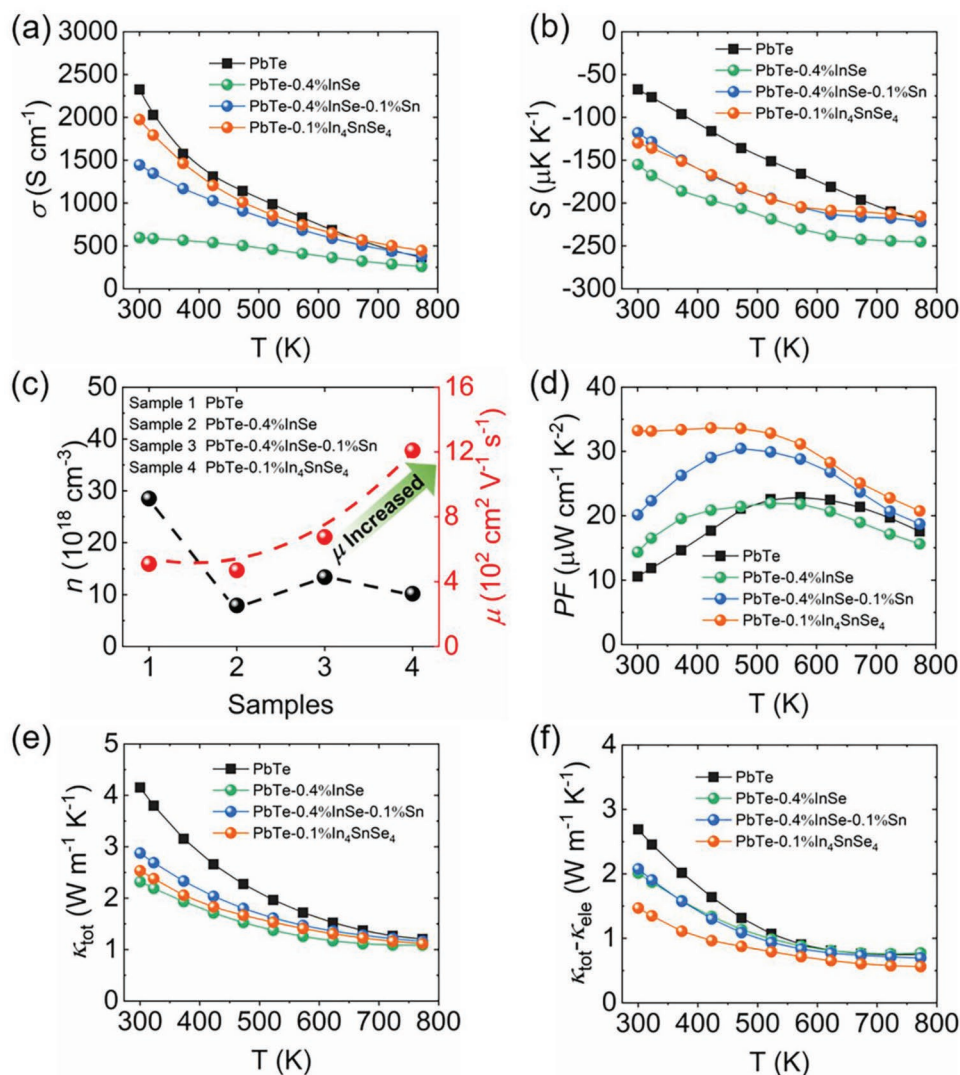
Figure 5. The comparison of thermoelectric properties among PbTe, PbTe-0.4%InSe, PbTe-0.4%InSe-0.1%Sn, and PbTe-0.1%In$_4$SnSe$_4$: a) electrical conductivity; b) Seebeck coefficient; c) carrier concentration and carrier mobility; d) power factor; e) total thermal conductivity; f) lattice thermal conductivity.

**ADVANCED
SCIENCE NEWS**

www.advancedsciencenews.com

**ADVANCED
ENERGY
MATERIALS**

www.advenergymat.de

transport properties. In Figure 5c, the carrier concentrations of the two samples are similar, while the carrier mobility surges abnormally, which is ≈674 cm^2 V^{-1} s^{-1} in PbTe-0.4%InSe-0.1%Sn but ≈1209 cm^2 V^{-1} s^{-1} in PbTe-0.1%In$_4$SnSe$_4$. The high carrier mobility of PbTe-0.1%In$_4$SnSe$_4$ leads to an increment in electrical conductivity as shown in Figure 5a. Consequently, the power factor is promoted from ≈20 µW cm^{-1} K^{-2} in PbTe-0.4%InSe-0.1%Sn to ≈33 µW cm^{-1} K^{-2} at 300 K in PbTe-0.1%In$_4$SnSe$_4$. Meanwhile, the heat transport in PbTe-0.1%In$_4$SnSe$_4$ is further impeded as shown in Figure 5e,f. The lattice thermal conductivity of PbTe-0.1%In$_4$SnSe$_4$ is ≈1.5 W m^{-1} K^{-1}, which is ≈30% lower than that of PbTe-0.4%InSe-0.1%Sn.

Combining with the above discussion of incomplete decomposition of In$_4$SnSe$_4$, it can be seen that the only difference between the two samples is that some undecomposed In$_4$SnSe$_4$ exists in PbTe-0.1%In$_4$SnSe$_4$. Therefore, the residual In$_4$SnSe$_4$ may rationalize the different properties between the two samples. **Figure 6**a exhibits the crystal structure of In$_4$SnSe$_4$, whose lattice parameter (≈12.66 Å) is approximately twice that of PbTe (≈6.45 Å), and both of them are crystallized in cubic structures. As shown in Figure 4g, it can be clearly seen that the boundary between the In$_4$SnSe$_4$ nano-precipitate and the PbTe matrix presents a semi-coherent interface (white dotted circle) due to the structural commonality of In$_4$SnSe$_4$ and PbTe. A schematic diagram of In$_4$SnSe$_4$ embedded in the PbTe matrix is shown in Figure 6b. The formation of semi-coherent interfaces can substantially weaken the scattering of carriers, compared to the InSe precipitates in PbTe-0.4%InSe-0.1%Sn. Simultaneously, the inlaid In$_4$SnSe$_4$ induces the distortion of the PbTe lattice and shortens the phonon relaxation time (τ) of PbTe, resulting in a lower lattice thermal conductivity in PbTe-0.1%In$_4$SnSe$_4$.[28] On the whole, the residual In$_4$SnSe$_4$ realizes the synergistic optimization of electrical and thermal transports.[29] In addition, the anomalous trend of electrical conductivity shown in Figure 1a can be explained by the combined effect of InSe, Sn, and undecomposed In$_4$SnSe$_4$.

To conclude, the carrier mobility (μ) and the inverse of the lattice thermal conductivity ($1/\kappa_{lat}$) are shown together in **Figure 7**a. It is visualized that the undecomposed In$_4$SnSe$_4$ can strike a balance between the transports of carriers and phonons. Compared with PbTe-0.4%InSe-0.1%Sn and
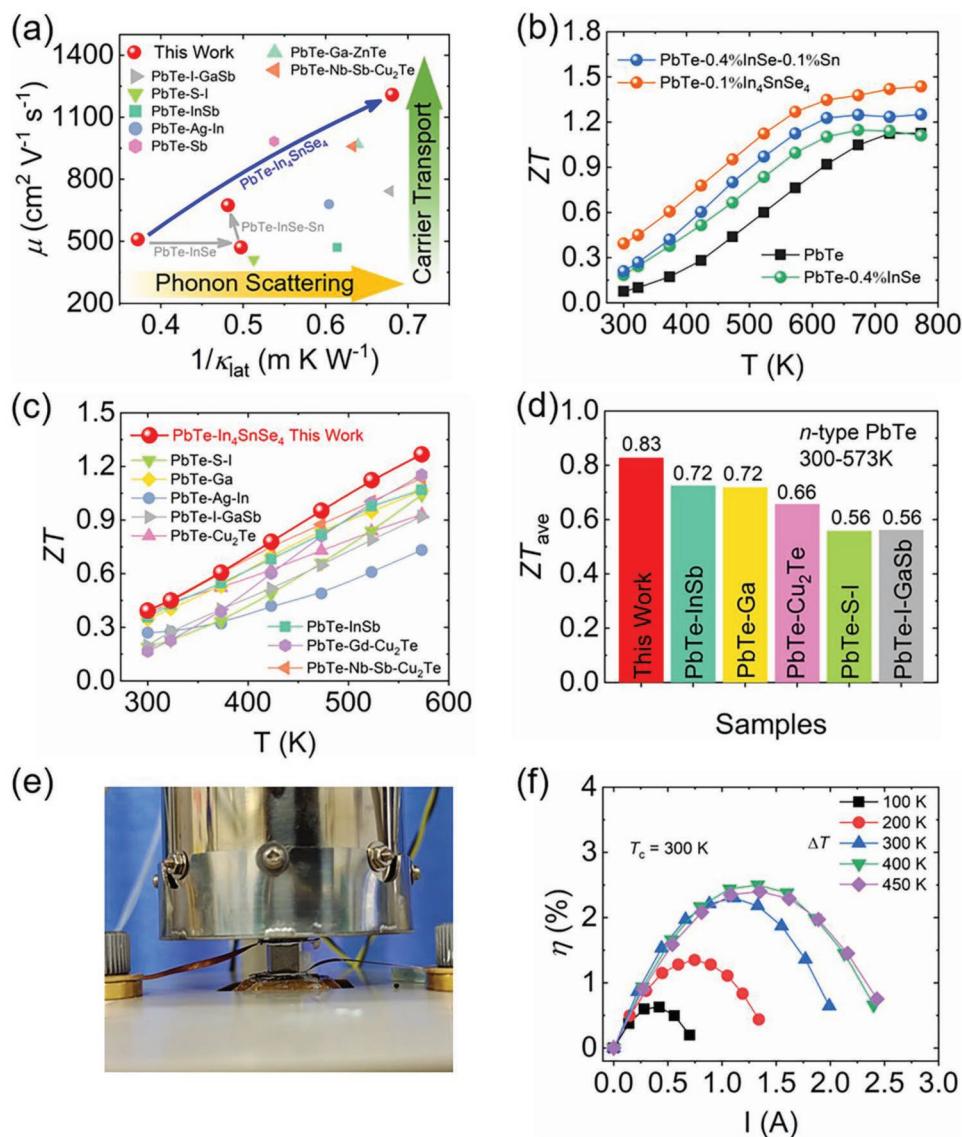
other n-type PbTe-based thermoelectric materials, the faster carrier mobility and further blocked phonons are presented in PbTe-0.1%In$_4$SnSe$_4$.[2c,7c,30] As a result, the ZT curve of PbTe-0.1%In$_4$SnSe$_4$ is more saturated than that of PbTe-0.4%InSe-0.1%Sn in Figure 7b. A high ZT value of ≈0.4 at room temperature and ZT_{ave} of ≈0.83 at 300–573 K are achieved, which is superior to other reported n-type PbTe as shown in Figure 7c,d.[2c,7c,18g,30b–d,31] Finally, based on the high-performance sample PbTe-0.1%In$_4$SnSe$_4$, a single-leg device is fabricated, and the maximum thermoelectric conversion efficiency (η) of ≈2.5% ($\Delta T \approx 400$ K) is obtained, as shown in Figure 7e,f.

3. Conclusion

In this work, an unstable additive In$_4$SnSe$_4$ with intrinsic low thermal conductivity was introduced into n-type PbTe. We experimentally observed the incomplete decomposition of In$_4$SnSe$_4$, during which ≈80% of In$_4$SnSe$_4$ dissolved into InSe and Sn, and ≈20% of undecomposed In$_4$SnSe$_4$ second phases remained in the PbTe matrix. By further conducting the thermoelectric performance analysis and Cs-corrected STEM characterizations, we discovered the synergistic effects of the partially decomposed In$_4$SnSe$_4$ on decoupling the electron and phonon transports in n-type PbTe. First, as the decomposition products, InSe alloying and the precipitates lowered the lattice thermal conductivity, and Sn enhanced the carrier mobility by occupying the intrinsic Pb vacancies. Second, the undecomposed In$_4$SnSe$_4$ was embedded into the PbTe matrix. The semi-coherent interfaces simultaneously expedited the carrier transport and blocked the phonons. Resultantly, the high performance in PbTe-0.1%In$_4$SnSe$_4$, with the room-temperature ZT of ≈0.4 and a state-of-the-art ZT_{ave} of ≈0.83 at 300–573 K were achieved. And an experimental maximum thermoelectric conversion efficiency (η) of ≈2.5% ($\Delta T \approx 400$ K) is obtained by the single-leg device. This work proved that the decomposition behavior of In$_4$SnSe$_4$ can significantly promote the thermoelectric properties in n-type PbTe. Moreover, the strategy of introducing unstable additives into thermoelectric materials proved effective. Based on the new strategy, more multi-element compounds with intrinsic low thermal conductivity
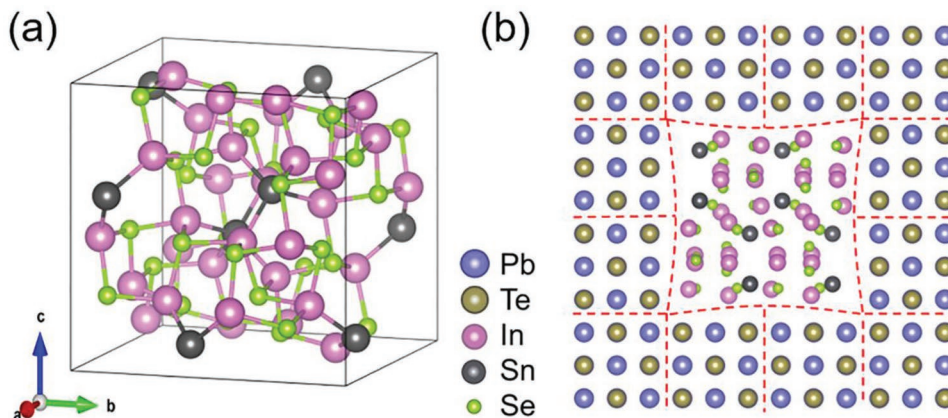
Figure 6. a) The crystal structure of In$_4$SnSe$_4$; b) the schematic diagram of the In$_4$SnSe$_4$ embedded in the PbTe matrix. The red dashed lines refer to the crystal lattice.

**ADVANCED
SCIENCE NEWS**

www.advancedsciencenews.com

**ADVANCED
ENERGY
MATERIALS**

www.advenergymat.de

Figure 7. The experimental figure of merit and power generation of PbTe-0.1%In$_4$SnSe$_4$: a) the synergistic optimization of carrier mobility and lattice thermal conductivity in this work (PbTe, PbTe-0.4%InSe, PbTe-0.4%InSe-0.1%Sn, PbTe-0.1%In$_4$SnSe$_4$) and other n-type PbTe samples (PbTe-I-GaSb,[30d] PbTe-S-I,[30b] PbTe-InSb,[2c] PbTe-Ag-In,[30c] PbTe-Sb,[30e] PbTe-Ga-ZnTe,[30a] and PbTe-Nb-Sb-Cu$_2$Te[7c]); b) the ZT values at 300–773 K of PbTe, PbTe-0.4%InSe, PbTe-0.4%InSe-0.1%Sn, and PbTe-0.1%In$_4$SnSe$_4$; c) the ZT values at 300–573 K of PbTe-0.1%In$_4$SnSe$_4$ and other n-type PbTe samples (PbTe-S-I,[30b] PbTe-Ga,[31b] PbTe-Ag-In,[30c] PbTe-I-GaSb,[30d] PbTe-Cu$_2$Te,[31a] PbTe-InSb,[2c] PbTe-Gd-Cu$_2$Te,[18 g] and PbTe-Nb-Sb-Cu$_2$Te[7c]); d) the ZT$_{ave}$ at 300–573 K of PbTe-0.1%In$_4$SnSe$_4$ and other n-type PbTe samples (PbTe-InSb,[2c] PbTe-Ga,[31b] PbTe-Cu$_2$Te,[31a] PbTe-S-I,[30b] and PbTe-I-GaSb[30d]); e) image of the power generation measurement for high performance PbTe-0.1%In$_4$SnSe$_4$ sample; f) experimental power generation efficiency (η) of PbTe-0.1%In$_4$SnSe$_4$.

are noteworthy to be selected as unstable additives. And the dynamic behaviors can also be utilized in other thermoelectric material systems by seeking additives that match the matrix, which possess a suitable decomposition temperature and rate, a similar crystal structure to the matrix, and so on.

Supporting Information

Supporting Information is available from the Wiley Online Library or from the author.

Acknowledgements

Conflict of Interest

The authors declare no conflict of interest.

Data Availability Statement

The data that support the findings of this study are available from the corresponding author upon reasonable request.

Keywords

[1] a) J. Mao, G. Chen, Z. Ren, *Nat. Mater.* **2021**, *20*, 454; b) B. Qin, D. Wang, L.-D. Zhao, *InfoMat* **2021**, *3*, 755; c) X.-L. Shi, J. Zou, Z.-G. Chen, *Chem. Rev.* **2020**, *120*, 7399; d) N. Dragoe, *Mater. Lab* **2022**, *1*, 220001.

[2] a) D. Liu, B. Qin, L.-D. Zhao, *Mater. Lab* **2022**, *1*, 220006; b) Q. Zhang, E. K. Chere, J. Sun, F. Cao, K. Dahal, S. Chen, G. Chen, Z. Ren, *Adv. Energy Mater.* **2015**, *5*, 1500360; c) J. Zhang, D. Wu, D. He, D. Feng, M. Yin, X. Qin, J. He, *Adv. Mater.* **2017**, *29*, 1703148; d) B. Qin, L.-D. Zhao, *Mater. Lab* **2022**, *1*, 220004; e) F. Zhang, X. Qiao, Q. Shi, X. Chao, Z. Yang, D. Wu, *J. Eur. Ceram. Soc.* **2021**, *41*, 368.

[3] a) L. Su, D. Wang, S. Wang, B. Qin, Y. Wang, Y. Qin, Y. Jin, C. Chang, L.-D. Zhao, *Science* **2022**, *375*, 1385; b) H. Wang, Y. Pei, A. D. LaLonde, G. J. Snyder, *Proc. Natl. Acad. Sci. USA* **2012**, *109*, 9705; c) Z. Liu, T. Hong, L. Xu, S. Wang, X. Gao, C. Chang, X. Ding, Y. Xiao, L. D. Zhao, *Interdiscip. Mater.* **2022**, https://doi.org/10.1002/idm2.12056.

[4] a) Y. Pei, X. Shi, A. D. LaLonde, H. Wang, L. Chen, G. J. Snyder, *Nature* **2011**, *473*, 66; b) Y. Pei, H. Wang, G. J. Snyde, *Adv. Mater.* **2012**, *24*, 6125; c) W. He, D. Wang, H. Wu, Y. Xiao, Y. Zhang, D. He, Y. Feng, Y.-J. Hao, J.-F. Dong, R. Chetty, L. Hao, D. Chen, J. Qin, Q. Yang, X. Li, J.-M. Song, Y. Zhu, W. Xu, C. Niu, X. Li, G. Wang, C. Liu, M. Ohta, S. J. Pennycook, J. He, J.-F. Li, L.-D. Zhao, *Science* **2019**, *365*, 1418; d) J. Wang, Y. Yu, J. He, J. Wang, B. Ma, X. Chao, Z. Yang, D. Wu, *ACS Appl. Energy Mater.* **2021**, *4*, 14608.

[5] a) J. P. Heremans, V. Jovovic, E. S. Toberer, A. Saramat, K. Kurosaki, A. Charoenphakdee, S. Yamanaka, G. J. Snyder, *Science* **2008**, *321*, 554; b) J. P. Heremans, B. Wiendlocha, A. M. Chamoire, *Energy Environ. Sci.* **2012**, *5*, 5510; c) Q. Zhang, H. Wang, W. Liu, H. Wang, B. Yu, Q. Zhang, Z. Tian, G. Ni, S. Lee, K. Esfarjani, G. Chen, Z. Ren, *Energy Environ. Sci.* **2012**, *5*, 5246.

[6] a) Z. Huang, L.-D. Zhao, *J. Mater. Chem. C* **2020**, *8*, 12054; b) B. Qin, D. Wang, W. He, Y. Zhang, H. Wu, S. J. Pennycook, L.-D. Zhao, *J. Am. Chem. Soc.* **2019**, *141*, 1141; c) L. Xu, G. Wu, R. Wang, Z. Yan, J. Cai, J. Yang, X. Wang, J. Luo, X. Tan, G. Liu, J. Jiang, *ACS Appl. Mater. Interfaces* **2022**, *14*, 14359; d) X. Qi, Y. Yu, X. Xu, J. Wang, F. Zhang, B. Zhu, J. He, X. Chao, Z. Yang, D. Wu, *Mater. Today Phys.* **2021**, *21*, 100507.

[7] a) K. Biswas, J. He, I. D. Blum, C.-I. Wu, T. P. Hogan, D. N. Seidman, V. P. Dravid, M. G. Kanatzidis, *Nature* **2012**, *489*, 414; b) W. Zhao, Z. Liu, Z. Sun, Q. Zhang, P. Wei, X. Mu, H. Zhou, C. Li, S. Ma, D. He, P. Ji, W. Zhu, X. Nie, X. Su, X. Tang, B. Shen, X. Dong, J. Yang, Y. Liu, J. shi, *Nature* **2017**, *549*, 247; c) H.-T. Liu, Q. Sun, Y. Zhong, C.-L. Xia, Y. Chen, X.-L. Shi, Z.-G. Chen, R. Ang, *Mater. Today Phys.* **2022**, *24*, 100677.

[8] a) T. Zhu, Y. Liu, C. Fu, J. P. Heremans, J. G. Snyder, X. Zhao, *Adv. Mater.* **2017**, *29*, 1605884; b) A. Bhui, T. Ghosh, K. Pal, K. S. Rana, K. Kundu, A. Soni, K. Biswas, *Chem. Mater.* **2022**, *34*, 3301; c) Y. Li, S. Yamamoto, K. Ahmad, Z. Almutairi, K. Koumoto, C. Wan,

[8] (cont.) *J. Mater. Chem. A* **2021**, *9*, 11674; d) M. Dutta, K. Pal, U. V. Waghmareb, K. Biswas, *Chem. Sci.* **2019**, *10*, 4905; e) M. Dutta, S. Matteppanavar, M. V. D. Prasad, J. Pandey, A. Warankar, P. Mandal, A. Soni, U. V. Waghmare, K. Biswas, *J. Am. Chem. Soc.* **2019**, *141*, 20293.

[9] a) C. Chang, D. Wang, D. He, W. He, F. Zhu, G. Wang, J. He, L.-D. Zhao, *Adv. Energy Mater.* **2019**, *9*, 1901334; b) B. Qin, D. Wang, X. Liu, Y. Qin, J.-F. Dong, J. Luo, J.-W. Li, W. Liu, G. Tan, X. Tang, J.-F. Li, J. He, L.-D. Zhao, *Science* **2021**, *373*, 556.

[10] Y. Xiao, Y. Wu, P. Nan, H. Dong, Z. Chen, Z. Chen, H. Gu, B. Ge, W. Li, Y. Pei, *Chem* **2020**, *6*, 523.

[11] S. Roychowdhury, T. Ghosh, R. Arora, M. Samanta, L. Xie, N. K. Singh, A. Soni, J. He, U. V. Waghmare, K. Biswas, *Science* **2021**, *371*, 722.

[12] A. Basit, J. Yang, Q. Jiang, J. Xin, X. Li, S. Li, S. Li, Q. Long, *J. Mater. Chem. A* **2018**, *6*, 23473.

[13] H. Xie, Y. Liu, Y. Zhang, S. Hao, Z. Li, M. Cheng, S. Cai, G. J. Snyder, C. Wolverton, C. Uher, V. P. Dravid, M. G. Kanatzidis, *J. Am. Chem. Soc.* **2022**, *144*, 9113.

[14] C.-F. Wu, T.-R. Wei, F.-H. Sun, J.-F. Li, *Adv. Sci.* **2017**, *4*, 1700199.

[15] a) M. Dutta, K. Pal, M. Etter, U. V. Waghmare, K. Biswas, *J. Am. Chem. Soc.* **2021**, *143*, 16839; b) H. Wang, H. Hu, N. Man, C. Xiong, Y. Xiao, X. Tan, G. Liu, J. Jiang, *Mater. Today Phys.* **2021**, *16*, 100298; c) Y. Wang, B. Qin, T. Hong, L. Su, X. Gao, D. Wang, L.-D. Zhao, *Acta Mater.* **2022**, *227*, 117681.

[16] Y. Qin, T. Hong, B. Qin, D. Wang, W. He, X. Gao, Y. Xiao, L.-D. Zhao, *Adv. Funct. Mater.* **2021**, *31*, 2102185.

[17] Z. Huang, D. Wang, C. Li, J. Wang, G. Wang, L.-D. Zhao, *J. Mater. Chem. A* **2020**, *8*, 4931.

[18] a) Y. Pei, Z. M. Gibbs, B. Balke, W. G. Zeier, G. J. Snyder, *Adv. Energy Mater.* **2014**, *4*, 1400486; b) E. S. Božin, C. D. Malliakas, P. Souvatzis, T. Proffen, N. A. Spaldin, M. G. Kanatzidis, S. J. L. Billinge, *Science* **2010**, *330*, 1660; c) Y. Xiao, L. Xu, T. Hong, H. Shi, S. Wang, X. Gao, X. Ding, J. Sun, L.-D. Zhao, *Energy Environ. Sci.* **2021**, *15*, 346; d) Y. Xiao, H. Wu, H. Shi, L. Xu, Y. Zhu, Y. Qin, G. Peng, Y. Zhang, Z.-H. Ge, X. Ding, L.-D. Zhao, *Adv. Energy Mater.* **2022**, *12*, 2200204; e) K. F. Hsu, S. Loo, F. Guo, W. Chen, J. S. Dyck, C. Uher, T. Hogan, E. K. Polychroniadis, M. G. Kanatzidis, *Science* **2004**, *303*, 818; f) Z. Chen, B. Ge, W. Li, S. Lin, J. Shen, Y. Chang, R. Hanus, G. J. Snyder, Y. Pei, *Nat. Commun.* **2017**, *8*, 13828; g) C. Qin, L. Cheng, Y. Xiao, C. Wen, B. Ge, W. Li, Y. Pei, *Mater. Today Phys.* **2021**, *17*, 100355.

[19] H. Shi, C. Guo, B. Qin, G. Wang, D. Wang, L.-D. Zhao, *J. Materiomics* **2022**, *8*, 982.

[20] a) H.-T. Liu, Q. Sun, Y. Zhong, Q. Deng, L. Gan, F.-L. Lv, X.-L. Shi, Z.-G. Chen, R. Ang, *Nano Energy* **2022**, *91*, 106706; b) H.-T. Liu, Q. Sun, Y. Zhong, C.-L. Xia, Y. Chen, Z.-G. Chen, R. Ang, *Chem. Eng. J.* **2022**, *428*, 132601.

[21] a) D. Sun, Y. Xiong, Y. Sun, I. Dabo, R. E. Schaak, *Chem. Mater.* **2017**, *29*, 1095; b) W. Meng, X. Wang, Y. Yan, J. Wang, *J. Phys. Chem. C* **2018**, *122*, 10360.

[22] J. Zhao, S. M. Islam, G. Tan, S. Hao, C. Wolverton, R. K. Li, M. G. Kanatzidis, *Chem. Mater.* **2017**, *29*, 1744.

[23] J. Zhao, S. M. Islam, S. Hao, G. Tan, X. Su, H. Chen, W. Lin, R. Li, C. Wolverton, M. G. Kanatzidis, *Chem. Mater.* **2017**, *29*, 8494.

[24] H.-J. Deiseroth, H. Pfeifer, *Z. Kristallogr. Cryst. Mater.* **1993**, *201*, 151.

[25] X. Lian, J. Wang, B. Ma, X. Chao, Z. Yang, F. Zhang, D. Wu, *J. Alloys Compd.* **2022**, *907*, 164416.

[26] a) H. Shi, D. Wang, Y. Xiao, L.-D. Zhao, *Aggregate* **2021**, *2*, e92; b) K. H. Lee, M.-W. Oh, H.-S. Kim, W. H. Shin, K. Lee, J.-H. Lim, J.-i. Kim, S.-i. Kim, *Inorg. Chem. Front.* **2019**, *6*, 1475.

[27] Y. Xiao, W. Li, C. Chang, Y. Chen, L. Huang, J. He, L.-D. Zhao, *J. Alloys Compd.* **2017**, *724*, 208.

[28] Y. Wu, Z. Chen, P. Nan, F. Xiong, S. Lin, X. Zhang, Y. Chen, L. Chen, B. Ge, Y. Pei, *Joule* **2019**, *3*, 1276.

[29] Y. Qin, Y. Xiao, L.-D. Zhao, *APL Mater.* **2020**, *8*, 010901.

**ADVANCED
SCIENCE NEWS**

www.advancedsciencenews.com

**ADVANCED
ENERGY
MATERIALS**

www.advenergymat.de

[30] a) Z.-Z. Luo, S. Cai, S. Hao, T. P. Bailey, Y. Luo, W. Luo, Y. Yu, C. Uher, C. Wolverton, V. P. Dravid, Z. Zou, Q. Yan, M. G. Kanatzidis, *Energy Environ. Sci.* **2022**, *15*, 368; b) B. Jia, Y. Huang, Y. Wang, Y. Zhou, X. Zhao, S. Ning, X. Xu, P. Lin, Z. Chen, B. Jiang, J. He, *Energy Environ. Sci.* **2022**, *15*, 1920; c) Y. Xiao, H. Wu, D. Wang, C. Niu, Y. Pei, Y. Zhang, I. Spanopoulos, I. T. Witting, X. Li, S. J. Pennycook, G. J. Snyder, M. G. Kanatzidis, L.-D. Zhao, *Adv. Energy Mater.* **2019**, *9*, 1900414; d) S. Sarkar, X. Hua, S. Hao, X. Zhang, T. P. Bailey, T. J. Slade,

P. Yasaei, R. J. Korkosz, G. Tan, C. Uher, V. P. Dravid, C. Wolverton, M. G. Kanatzidis, *Chem. Mater.* **2021**, *33*, 1842; e) C. Wang, X. Zhao, S. Ning, Q. Tao, Y. Tang, Z. Chen, J. Wu, X. Sua, X. Tang, *Mater. Today Energy* **2022**, *25*, 100962.

[31] a) Y. Xiao, H. Wu, W. Li, M. Yin, Y. Pei, Y. Zhang, L. Fu, Y. Chen, S. J. Pennycook, L. Huang, J. He, L.-D. Zhao, *J. Am. Chem. Soc.* **2017**, *139*, 18732; b) X. Su, S. Hao, T. P. Bailey, S. Wang, I. Hadar, G. Tan, T.-B. Song, Q. Zhang, C. Uher, C. Wolverton, X. Tang, M. G. Kanatzidis, *Adv. Energy Mater.* **2018**, *8*, 1800659.